

Soliton instability and fold formation in laterally compressed few-layer graphene

Amauri Libério de Lima¹, Lucas A. M. Müssnich², Taíse M. Manhabosco¹,
Hélio Chacham³, Ronaldo J. C. Batista¹, and Alan Barros de Oliveira¹

¹ Departamento de Física, Universidade Federal de Ouro Preto, Ouro Preto, MG, 35400-000, Brazil.

² Departamento de Física-Matemática, Universidade de São Paulo, São Paulo, SP, 05314-970, Brazil.

³ Departamento de Física, Universidade Federal de Minas Gerais, Belo Horizonte, MG, 30123-970, Brazil.

(Dated: July 7, 2021)

We investigate – through simulations and analytical calculations – the consequences of uniaxial lateral compression applied to the upper layer of few-layer graphene. The simulations of compressed graphene show that strains larger than 2.8 % induce soliton-like deformations that further develop into large, mobile folds. Such folds were indeed experimentally observed in graphene and other solid lubricants two-dimensional materials. Interestingly, in the soliton-fold regime the shear stress decreases with the strain s , initially as $s^{-2/3}$ and rapidly going to zero. Such instability is consistent with the recently observed negative dynamic compressibility of two-dimensional materials. We also predict that the curvatures of the soliton-folds are given by $r_c = \delta\sqrt{\beta/2\alpha}$, where $1 \leq \delta \leq 2$, and β and α are respectively related to the layer bending modulus and to the exfoliation energy of the material. This finding might allow experimental estimates of the β/α ratio of two-dimensional materials from fold morphology.

I. INTRODUCTION

Graphene has gained much attention from the scientific community since its discovery because of its unique features. For example, it has been considered as a possible building block for circuit components due to its particular electronic properties. Ideally, deposited graphene should be perfectly flat. However, although graphene has one of the highest known Young's modulus, it has small bending modulus.¹ In real applications, graphene sheets commonly present ripples and folds,^{2–5} which may change its electronic structure. For example, theoretical studies suggest that folded graphene under external magnetic fields act as interferometer: it suffers the interference due to the interplay between gauge fields created by the fold and the external fields in the region of the fold.⁶ Zheng *et al.* have shown that the calculated Young's modulus, tensile strength, and fracture strain of folded graphene are comparable to those of graphene, while the compressive strength and strain are much higher than those of planar graphene.⁷

Folds have been observed in several conditions and in a variety of forms. They were seen in the top layers of graphite^{8,9} whereas edge folds in suspended graphene have been reported as well.^{10–14} By concomitantly applying compressive and shear stresses through an atomic force microscopy tip upon few layer graphene, Barboza and collaborators obtained structures which appear to be single- and multi-folded graphene.¹⁵ Multiply folded graphene – termed grafold by Kim and coworkers¹⁶ – were indeed confirmed to exist and, not surprisingly, its novel electronic structure can be quite different in comparison to the flat graphene.^{16–18}

Theoretical models suggest that folds in graphene can change its chemical affinity, since curvatures induce deformations in the σ -bonds of the lattice. Such out-of-plane deformed bonds could transfer charges to π -orbitals which induce localized dipole moments in the graphene

surface.¹⁹ This property could lead to localized selective functionalization of atoms and molecules. For example, Tozzini and collaborators have shown that storage (through adsorption) and release of hydrogen can in principle be obtained by exploiting and controlling the corrugation of individual layers of graphene.²⁰ Storage of molecules can also be achieved by wrapping chemical species into graphene folds as sandwiches.^{16,21,22}

Given the relevance of graphene folds, it is important to understand the physics behind the folding process. Bending orientation, defects, and contamination are probably determinant on such a process.^{23–28} In this work we investigate – through molecular dynamics and theoretical calculations – laterally compressed graphene bilayers. At low strains we observed soliton-like structures that evolve into mobile folds with increasing strains. Our results include the derivation of curvature radii of some of the main structures formed during compression in terms of exfoliation and bending energies, α and β , respectively. Our results can be applied to any solid lubricant, such as molybdenum disulfide and hexagonal boron nitride .

This work goes as follows. In Section II we describe the molecular dynamics methodology and the main fold structures that result from the simulations. In Section III we develop analytical models for the fold structures. Section IV is destined to discuss the simulation results and comparisons with the analytical models. In Section V we present our conclusions.

II. MOLECULAR DYNAMICS: METHODOLOGY AND FOLD STRUCTURES

Molecular dynamics techniques were used as implemented in the package LAMMPS.²⁹ Carbon atoms were modeled classically using the adaptive intermolecular reactive empirical bond order (AIREBO) potential for the C-C interaction.³⁰ Our system is composed of two

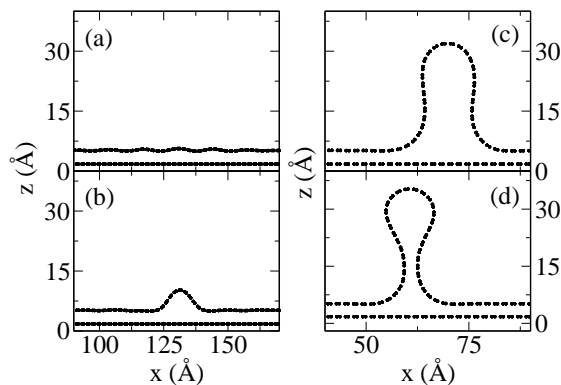


FIG. 1: Projection of the graphene bilayer into the xz plane obtained through simulations. (a) The moment immediately before the soliton formation at strain $s = 2.8\%$ (see Sec. IV for the definition of the strain). (b) The soliton structure and (c) the structure we termed as *standing fold*, which appear at $s = 27.5\%$. (d) The structure which appear at approximately $s = 28\%$. We named it as *standing collapsed fold*.

graphene layers, each one containing 1600 atoms. The bottom layer was kept “frozen” during all simulations, i.e., the resultant force on every atom of such layer was set to zero. Both ends of the top layer were also maintained frozen: the resultant forces acting upon 32 atoms of each extrema were kept zero in all simulations. Periodic boundary condition was used in the y direction, while directions x and z were finite. The dimensions of the layers were 207.0 and 18.1 Å in the x and y directions, respectively. The equilibrium distance between layers was found to be around 3.4 Å.

Simulations were performed in the canonical ensemble. The Nosé-Hoover thermostat^{31,32} as implemented by Shinoda and collaborators³³ was used in order to keep the temperature $T = 10$ K. The timestep used was 0.001 ps.

Compressive strain in the upper layer was imposed along the x direction by moving one of its frozen edges towards the another edge at constant velocity $v = dx/dt = 0.1$ Å/ps in the x direction. By increasing the strain, different structures are formed in the upper layer. Here we focus on those shown in Fig. 1. In Fig. 1(a) it is possible to see the xz projection of the upper layer in the moment immediately before a soliton-like structure appears. The soliton is shown in the Fig. 1(b). By further increasing s , two distinct structures appear in sequence. The first is the *standing fold*, shown in Fig. 1(c). The second is the *standing collapsed fold*, as seen in Fig. 1(d). For studying such structures, we developed theoretical models which are detailed in the next section.

III. ANALYTICAL MODEL

Our model consists of a continuum 2D material, ideally deposited on a substrate that is parallel to the xy

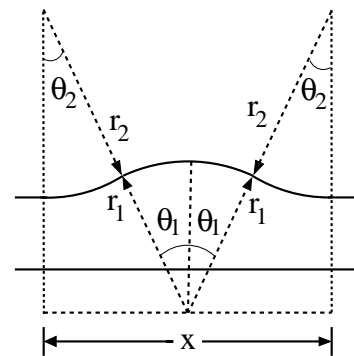


FIG. 2: Model for the soliton formation. r_1 and r_2 correspond to the top and basis radii, respectively, along with its corresponding angles, θ_1 and θ_2 .

plane. Wrinkles may appear parallel to the y direction, such that the local height z is a function of x only. The 2D material is incompressible but can be bent, with a bending modulus β defined such that the curvature energy per unit length, for a given curvature radius r , is given by $e_C = \beta/r^2$. We also consider that the binding energy per unit area between the 2D material and the substrate is given by $e_S = \alpha$.

A. The soliton structure

Let us first consider the soliton-like structure shown in Fig. 1(b). We model such structure with three circle segments as shown in Fig. 2. Considering the continuum model described above, the formation energy per unit length (along y) of such a soliton is given by

$$\epsilon = 2\alpha(r_1\theta_1 + r_2\theta_2) + 2\beta \left(\frac{\theta_1}{r_1} + \frac{\theta_2}{r_2} \right). \quad (1)$$

As a result of the soliton formation, the 2D material will have an apparent reduction in length, along x , of magnitude μ . From Fig. 2, μ is given by

$$\mu = 2(r_1\theta_1 + r_2\theta_2) - 2(r_1 \sin \theta_1 + r_2 \sin \theta_2), \quad (2)$$

If we consider small angles θ_1 and θ_2 , we can approximate Eq. (2) as

$$\mu \approx \frac{r_1\theta_1^3}{3} + \frac{r_2\theta_2^3}{3}. \quad (3)$$

Defining variables $q_i \equiv 2\beta\theta_i/r_i$ and $t_i \equiv 2\alpha r_i\theta_i$, with $i = 1, 2$, Eqs. (1) and (3) can be rewritten as

$$\epsilon = t_1 + t_2 + q_1 + q_2 \quad (4)$$

and

$$\mu = \frac{1}{24\alpha^2\beta} (q_1 t_1^2 + q_2 t_2^2). \quad (5)$$

The profile of the soliton can be found by minimizing its energy, Eq. (4), with $\mu = \text{constant}$. We find

$$t_1 = t_2 = (24\alpha^2\beta\mu)^{1/3} \quad \text{and} \quad q_1 = q_2 = \frac{1}{2}t_1. \quad (6)$$

Equations (6) lead to

$$r_1 = r_2 = \sqrt{2} \sqrt{\frac{\beta}{\alpha}} \quad (7)$$

$$\theta_1(\mu) = \theta_2(\mu) = \left(\frac{3}{2} \sqrt{\frac{\alpha}{2\beta}} \right)^{1/3} \mu^{1/3} \quad (8)$$

$$\epsilon(\mu) = 3 (24\alpha^2\beta)^{1/3} \mu^{1/3} \quad (9)$$

$$l(\mu) = 4 \left(\frac{3\beta}{\alpha} \right)^{1/3} \mu^{1/3}. \quad (10)$$

From Eqs. (7)-(10) we see that the soliton radii r_1 and r_2 are independent of μ (thus must be strain independent), whereas the angles θ_1 and θ_2 scale with $\mu^{1/3}$. This interesting behavior suggests that for $\mu \rightarrow 0$ the soliton localizes and disappears without “flattening”. Another interesting behavior is that of the tension f (force per unit length) necessary to maintain the soliton at a given μ . From Eq. (9), we obtain

$$f(\mu) = -d\epsilon/d\mu = K\mu^{-2/3}, \quad (11)$$

with $K = -(24\alpha^2\beta)^{1/3}$. That is, the magnitude of f reduces with increasing soliton size, and it tends to infinity as the soliton disappears.

B. The standing fold structure

For larger values of compressive strain, the soliton structure evolves to the pattern shown in Fig. 1(c), and schematically shown in Fig. 3. We model this structure as follows. The profile of the top part is composed by a semi circle with radius R_1 . A stem is formed by two straight lines with length h , and the basis is formed by quarter circles with radii R_2 . The formation energy of such a structure is given by

$$E = [\pi (R_1 + R_2) + 2h] \alpha + \beta\pi \left(\frac{1}{R_1} + \frac{1}{R_2} \right). \quad (12)$$

The net length to form this structure can be written as

$$\mu = (\pi - 2)(R_1 + R_2) + 2h. \quad (13)$$

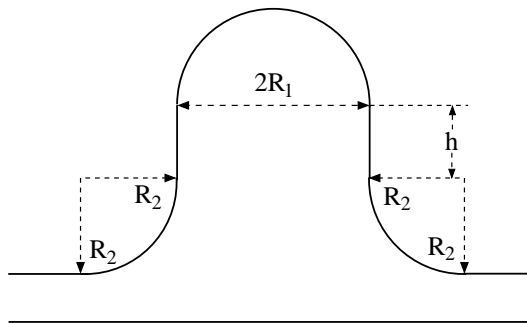


FIG. 3: Model for the *standing fold* structure. It has a top part modeled as a semi-circle with radius R_1 connected to the basis (quarter circles with radius R_2) by straight lines with length h .

Equations (12) and (13) reduce to

$$E = \alpha [\mu + 2 (R_1 + R_2)] + \beta\pi \left(\frac{1}{R_1} + \frac{1}{R_2} \right). \quad (14)$$

After minimizing Eq. (14) with respect to R_1 and R_2 with μ constant one obtains

$$R_1 = R_2 = \sqrt{\frac{\pi}{2}} \sqrt{\frac{\beta}{\alpha}}. \quad (15)$$

C. The standing collapsed fold structure

By further increasing the strain, the next type of structure observed for compressed graphene is schematically shown in Fig. 4. It corresponds to the structure shown in Fig. 1(d) obtained through simulations. We call this structure as *standing collapsed fold*. We modeled such an structure as an arc of circle of radius \mathcal{R}_1 , forming the top of the structure, which is connected to the basis by arcs of circle of radius \mathcal{R}_2 . $g_1(\mathcal{R}_1, \phi) = \mathcal{R}_1\phi$ and $g_2(\mathcal{R}_2, \psi) = \mathcal{R}_2\psi$ are the functions which define the head and the basis curves in polar coordinates, respectively. g_1 and g_2 intercept each other at the point P. In this sense, $g_1(\mathcal{R}_1, \phi = \gamma) = g_2(\mathcal{R}_2, \psi = \theta)$. Since $\gamma = \pi/2 - \theta$, we find that

$$\theta = \frac{\mathcal{R}_1\pi}{2(\mathcal{R}_1 + \mathcal{R}_2)}. \quad (16)$$

The formation energy is given by

$$\mathcal{E} = (\pi + 2\theta) \left[(\mathcal{R}_1 + \mathcal{R}_2) \alpha + \left(\frac{1}{\mathcal{R}_1} + \frac{1}{\mathcal{R}_2} \right) \beta \right]. \quad (17)$$

The variable θ can be eliminated from Eq. (17) with help of Eq. (16). Thus the energy reduces to

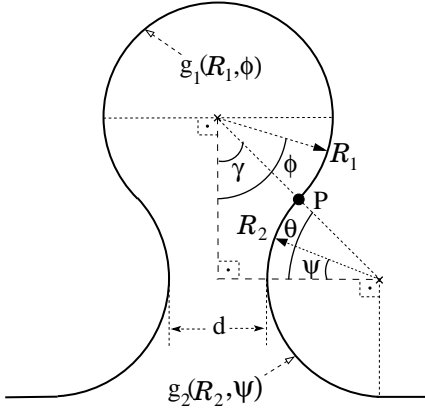


FIG. 4: The proposed model for the *standing collapsed fold*. The top and the basis are arcs of circle with radii R_1 and R_2 , respectively.

$$\mathcal{E} = \alpha\pi(2\mathcal{R}_1 + \mathcal{R}_2) + \beta\pi\left(\frac{1}{\mathcal{R}_1} + \frac{2}{\mathcal{R}_2}\right). \quad (18)$$

By minimizing with respect to \mathcal{R}_1 and \mathcal{R}_2 , i.e., performing $\partial\mathcal{E}/\partial\mathcal{R}_1 = 0$ and $\partial\mathcal{E}/\partial\mathcal{R}_2 = 0$, one finds

$$\mathcal{R}_1 = \frac{\sqrt{2}}{2}\sqrt{\frac{\beta}{\alpha}} \quad \text{and} \quad \mathcal{R}_2 = \sqrt{2}\sqrt{\frac{\beta}{\alpha}}. \quad (19)$$

It is possible to calculate the length of the rope, \mathcal{L} , detached from the substrate as a function of α and β . By simple inspection of Fig. 4 we see that

$$\mathcal{L} = (\pi + 2\theta)(\mathcal{R}_1 + \mathcal{R}_2). \quad (20)$$

Once $\mathcal{R}_2 = 2\mathcal{R}_1$, Eq. (16) gives $\theta = \pi/6$. This result, along with Eqs. (19) and (20), gives

$$\mathcal{L} = 2\sqrt{2}\pi\sqrt{\frac{\beta}{\alpha}}. \quad (21)$$

Another important result we can derive from this model is the minimum distance between the base arcs d . From Fig. 4, we find that

$$d = 2[(\mathcal{R}_1 + \mathcal{R}_2)\cos\theta - \mathcal{R}_2] = \frac{\sqrt{2}}{2}(3\sqrt{3} - 4)\sqrt{\frac{\beta}{\alpha}}, \quad (22)$$

where we have used Eq. (19) and $\theta = \pi/6$.

IV. SIMULATION RESULTS

We define the compressive strain in the upper layer as $s(t) = vt/L_x$, where L_x is the dimension of the layer in

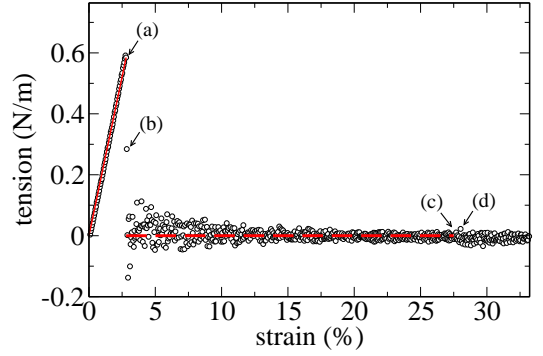


FIG. 5: Tension in the upper graphene layer as a function of the induced strain s . At $s = 0$ the tensile force upon the graphene layer is zero. By increasing s the graphene behaves as an elastic medium until the soliton formation at $s = 2.8\%$. At this point, internal forces are released which causes the discontinuity seen in the figure. For $s > 2.8$ the curve decays as $s^{-2/3}$ which is explained by our theoretical model (see Sec. III). Arrows (a)-(d) correspond to the instants where the structures seen in Fig. 1 appear.

the x direction and t is the time. In this sense, the strain is zero at the initial time, $t = 0$, and it is maximum ($s = 100\%$) when $vt = L_x$.

In order to characterize the structures shown in Fig. 1, namely, the soliton, the *standing fold* and the *standing collapsed fold*, we calculated the tension versus the compressive strain in the upper layer. The tension was calculated as $P_{xx}L_y$, where P_{xx} is the virial contribution for the component of the stress tensor in the x direction, and L_y is the dimension of the simulation box in the y direction. P_{xx} is given by

$$P_{xx} = \frac{1}{V} \sum_{i=1}^N x^i f_x^i \quad (23)$$

where V is the volume of the simulation box, N is the number of particles, x^i is the coordinate x of particle i , and f_x^i is the component of the resultant force acting on particle i in the x direction.

Our tension vs. strain results are summarized in the Fig. 5. Arrows (a)-(d) indicate the instants where the structures shown in Fig. 1 appear. In the first stages of compression, the layer behaves elastically, with linear response to the applied strain. The straight, continuous line corresponds to a linear fitting through the data whose angular coefficient was found to be 0.21 N/m. After reaching a maximum tension τ value, at $s = 2.8\%$, the soliton appears, releasing internal forces, which explains the discontinuity in the stress-strain curve. Further increasing s , the tension decays towards zero with a $s^{-2/3}$ dependence. Such a dependence is explained by our analytical model, Eq. (11). The fitting for $s > 2.8\%$ (dashed line) was made by using a function in the form $\tau = \kappa s^{-2/3}$, where $\kappa = 0.003$ N/m.

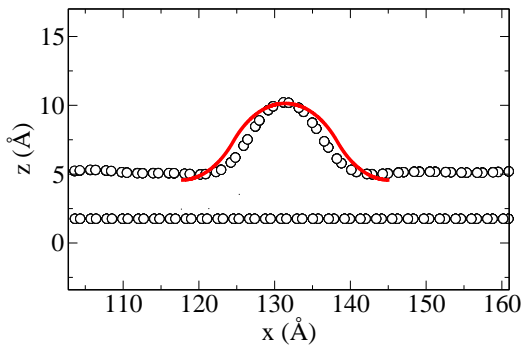


FIG. 6: Dots: the soliton as obtained in our simulations. Continuous curve: result from the soliton model (Eqs. (7) and (8)).

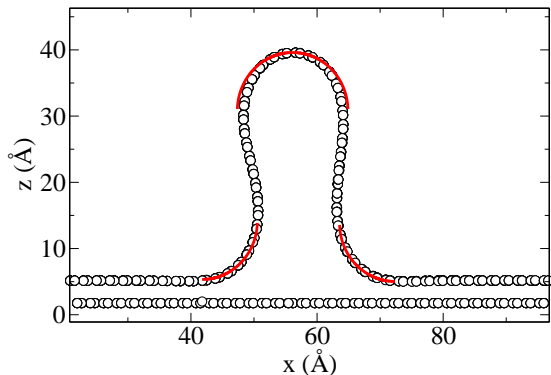


FIG. 7: Dots: the *standing fold* structure, as obtained in the simulations (also seen in Fig. 1(c)). Continuous curves: curvature radii as obtained from the analytical model, see Eq. (15) and relation (24).

We have also compared predictions of our theoretical models with the results from the simulations. Figures 6, 7, and 8 show the structures seen in Figs. 1(b), 1(c), and 1(d), respectively, superimposed with continuous curves that correspond to curvatures as obtained by our models.

The results from the models depend on the binding energy and the bending modulus of the graphene (α and β , respectively), always in the form $\sqrt{\beta/\alpha}$, which turned to be an *intrinsic length scale*. There have been several attempts to determine the graphite binding energy, both experimentally^{34–36} and theoretically.^{37–41} To the best of our knowledge, the most recent, direct graphite binding energy measurement is given by Liu *et al.*, who have obtained $\alpha = 31$ meV/atom.⁴² For the graphene bending modulus, the most direct measurement is due to Barboza and collaborators¹ who have found $\beta = 1.64$ eVÅ²/atom. Thus, the *intrinsic length scale* seen in our models is given by

$$\sqrt{\beta/\alpha} = 7.0 \text{ \AA}. \quad (24)$$

The soliton model (Fig. 2) predicts that the radii of both basis and top must be the same. We have found

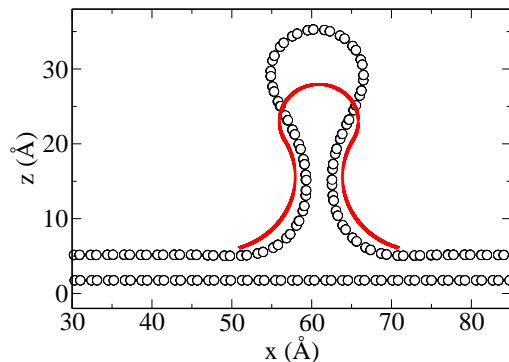


FIG. 8: Dots: *collapsed standing fold* structure, also seen in Fig. 1(d). Continuous curve: analytical model, see Eqs. (19) and (24).

such curvature radii $r_1 = r_2 = 9.9$ Å [see Eq. (7)]. In order to compare the model and simulation results, we have used Eq. (8) with $\mu = 3.0$ Å (estimated from simulations) for drawing the soliton as predicted by our model. This leads to $\theta = 44^\circ$. The resulting curve is seen in Fig. 6 as a line, while the circles mark the position of carbon atoms, obtained by simulations.

Figure 7 shows the *standing fold* structure as obtained by simulations. This structure is seen when the strain s is around 27.5 % (see Fig. 5). We have modeled such a structure as having circumference arcs in the top (with radius R_1) and in the basis (radius R_2) (see Fig. 3). Top and basis are connected by straight lines with length h . We obtained $R_1 = R_2 = 8.8$ Å [see Eq. (15)]. Figure 7 shows the model predictions (lines) along with simulations results (circles). We see that in spite the simplicity of the model it gives reasonable results compared to simulations without the need of any information from it other than the bending modulus and the binding energy values. Therefore, such models can be used to make predictions on the fold geometry of other solid lubricants and vice-versa, that is, to predict the value of the ratio β/α based purely on fold geometry.

Finally, Fig. 8 shows the *standing collapsed fold*, which was modeled as having R_1 for the top radius and R_2 for the basis (as shown in Fig. 4). We concluded that the condition which minimizes the energy of the collapsed fold is $R_2 = 2R_1$, given by Eqs. (19). Our findings are $R_1 = 4.95$ Å and $R_2 = 9.9$ Å. Note that the laterals of this structure tend to approach the bilayer distance (around 3.4 Å) for big strains as expected. The result from the model for such a distance is $d = 5.9$ Å [see Eq. (22)], which lies in the same order of magnitude. Since we have not considered van der Waals interaction between layers, it is not surprising we have found a bigger value for such a distance than the expected value of ~ 3.4 Å.

It is worth to mention we have found from the *standing collapsed fold* model an expression for the length of the layer which is detached from the substrate as a function of α and β , in the moment it is formed [Eq. (21)]. We estimate such a value from simulation as 84 Å, while Eq.

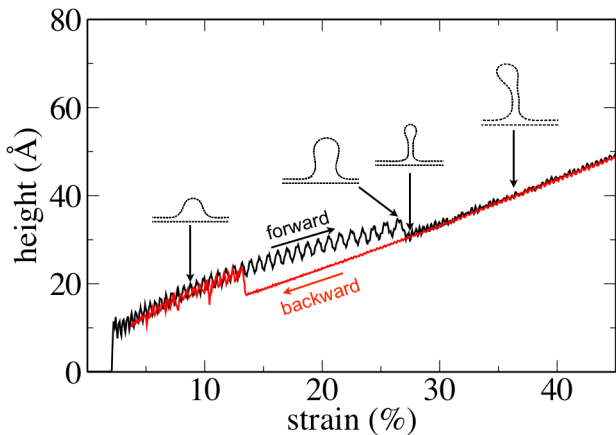


FIG. 9: (color online) Height of the fold structures, relative to the unstrained upper layer, versus the induced strain. The black curve refers to simulations with increasing strain, and red curve refers to simulations with decreasing strain. The *standing collapsed fold* is formed at $s = 28\%$ in the increasing strain simulation, but it persists for strains up to $s = 13.4\%$ in the decreasing strain simulation, evidencing a hysteresis effect.

(21) gives 62 \AA .

In order to investigate the stability of the *standing collapsed fold* structure, we proceeded as follows. As stated in Sec. II, strain was induced in the x direction of the upper layer by moving one of its extremities towards the opposite one at constant velocity. After a certain maximum strain, we inverted the movement direction, keeping the velocity modulus, which continuously reduces the strain. During this “forward-backwards” process, we monitor the height of the structures in relation to the upper layer against the induced strain. The results are summarized in Fig. 9. From this figure, we see all the stages approached in this work, namely, the soliton (see the jump at around $s = 2.8\%$ which characterizes its appearance) and its continuation until the *standing fold* takes place at around $s = 27.5\%$. At $s = 28\%$ we observe the transition from *standing fold* to *standing collapsed fold* with linear dependence between height and strain for $s > 28$

%. When the direction of the movement is inverted, the *standing collapsed fold* becomes stable for strains below $s = 28\%$. Indeed, the “uncollapsing” transition occurs at $s = 13.4\%$. Figure 9 has the characteristics of a hysteresis curve, in which the state of the system depends not only to the strain at a certain time but also to its history.

V. CONCLUSIONS

This work is an investigation – through molecular dynamics and analytical calculations – of a laterally compressed graphene monolayer atop uncompressed graphene (simulating an uncompressed graphite surface). Under compression, several structures appear in the top graphene layer. Three structures can be clearly identified: the soliton, the *standing fold*, and the *standing collapsed fold* structures. We propose models for each of such structures, and we have determined curvature radii for those structures in terms of α and β , the exfoliation and bending energies, respectively. Our models indicate that all structures have characteristic radii in terms of $\sqrt{\beta/2\alpha}$, as seen in Eqs. (7), (15), and (19). This result is general and can be applied to other solid lubricants, like MoS_2 , talc, and hexagonal boron nitride, for example, to estimate the ratio β/α from fold morphology. We have also found that the *standing collapsed fold* shows bi-stability in relation to the strain s , depending on the path for achieving critical strains. Upon increasing strain, such structure appears at $s = 28\%$. Once it appears, if the strain is decreased, the *standing collapsed fold* remains stable until $s = 13.4\%$, showing a hysteresis behaviour.

ACKNOWLEDGMENTS

We thank for financial support from the Brazilian science agencies CNPq, CAPES and FAPEMIG. This work is also partially supported by the project INCT-Nanomateriais de Carbono.

¹ A. P. M. Barboza, H. Chacham, and B. R. A. Neves, Phys. Rev. Lett. **102**, 025501 (2009).
² A. L. V. de Parga, F. Calleja, B. Borca, M. C. G. Passeggi, J. J. Hinarejos, F. Guinea, , and R. Miranda, Phys. Rev. Lett. **100**, 056807 (2008).
³ A. T. N’Diaye, S. Bleikamp, P. J. Feibelman, and T. Michely, Phys. Rev. Lett. **97**, 215501 (2006).
⁴ C. Lui, L. Liu, K. Mak, G. Flynn, and T. Heinz, Nature (London) **462**, 339 (2009).
⁵ A. C. Neto, F. Guinea, N. Peres, K. Novoselov, and A. Geim, Rev. Mod. Phys. **81**, 109 (2009).
⁶ D. Rainis, F. Taddei, M. Polini, G. León, F. Guinea, and V. I. Fal’ko, Phys. Rev. B **83**, 165403 (2011).

⁷ Y. Zheng, N. Wei, Z. Fan, L. Xu, and Z. Huang, Nanotechnology **22**, 405701 (2011).
⁸ H. Hiura, T. W. Ebbesen, J. Fujita, K. Tanigaki, and T. Takada, Nature (London) **367**, 148 (1994).
⁹ H.-V. Roy, C. Kallinger, and K. Sattler, Surf. Sci. **1**, 407 (1998).
¹⁰ J. C. Meyer, A. K. Geim, M. I. Katsnelson, K. S. Novoselov, T. J. Booth, and S. Roth, Nature (London) **446**, 60 (2007).
¹¹ J. H. Warner, M. H. Rummeli, T. Gemming, B. Büchner, and G. A. D. Briggs, Nano Lett. **9**, 102 (2009).
¹² J. Y. Huang, F. Ding, B. I. Yakobson, P. Lu, L. Qi, and J. Li, Proc. Natl. Acad. Sci. USA **106**, 10103 (2009).

- ¹³ Z. Liu, K. Suenaga, P. J. F. Harris, and S. Iijima, *Phys. Rev. Lett.* **102**, 015501 (2009).
- ¹⁴ J. Zhang, J. Xiao, X. Meng, C. Monroe, Y. Huang, and J.-M. Zuo, *Phys. Rev. Lett.* **104**, 166805 (2010).
- ¹⁵ A. P. M. Barboza, H. Chacham, C. K. Oliveira, T. F. D. Fernandes, E. H. M. Ferreira, B. S. Archanjo, R. J. C. Batista, A. B. de Oliveira, and B. R. A. Neves, *Nano Lett.* **12**, 2313 (2012).
- ¹⁶ K. Kim, Z. Lee, B. D. Malone, K. T. Chan, B. Alemán, W. Regan, W. Gannett, M. F. Crommie, M. L. Cohen, and A. Zettl, *Phys. Rev. B* **83**, 245433 (2011).
- ¹⁷ W. Zhu, T. Low, V. Perebeinos, A. A. Bol, Y. Zhu, H. Yan, J. Tersoff, and P. Avouris, *Nano Lett.* **12**, 3431 (2012).
- ¹⁸ Y. Xie, Y. Chen, X. L. Wei, and J. Zhong, *Phys. Rev. B* **86**, 195426 (2012).
- ¹⁹ J. Feng, L. Qi, J. Huang, and J. Li, *Phys. Rev. B* **80**, 165407 (2009).
- ²⁰ V. Tozzini and V. Pellegrini, *J. Phys. Chem. C* **115**, 25523 (2011).
- ²¹ J. M. Yuk, K. Kim, B. Alemán, W. Regan, J. H. Ryu, J. Park, P. Ercius, H. M. Lee, A. P. Alivisatos, M. F. Crommie, J. Y. Lee, , and A. Zettl, *Nano Lett.* **11**, 3290 (2011).
- ²² M. Monthieux and E. Flahaut, *Mater. Sci. Eng. C* **27**, 1096 (2007).
- ²³ L. Qi, J. Y. Huang, J. Feng, and J. Li, *Carbon* **48**, 2354 (2010).
- ²⁴ J. S. Bunch, *Nat. Nanotechnol.* **6**, 331 (2011).
- ²⁵ N. Su, M. Liu, and F. Liu, *Nano Res.* **4**, 1242 (2011).
- ²⁶ A. L. J. Pang, V. Sorkin, Y.-W. Zhang, and D. J. Srolovitz, *Phys. Lett. A* **376**, 973 (2012).
- ²⁷ A. Catheline, *Soft Matter* **8**, 7882 (2012).
- ²⁸ L. Ortolani, E. Cadelano, G. P. Veronese, C. D. E. Boschi, E. Snoeck, L. Colombo, and V. Morandi, *Nano Lett.* **12**, 5207 (2012).
- ²⁹ S. J. Plimpton, *J. Comp. Phys.* **117**, 1 (1995).
- ³⁰ S. J. Stuart, A. B. Tutein, and J. A. Harrison, *J. Chem. Phys.* **112**, 6472 (2000).
- ³¹ S. Nosé, *J. Chem. Phys.* **81**, 511 (1984).
- ³² W. G. Hoover, *Phys. Rev. A* **31**, 1695 (1985).
- ³³ W. Shinoda, M. Shiga, and M. Mikami, *Phys. Rev. B* **69**, 134103 (2004).
- ³⁴ L. A. Girifalco and R. A. Lad, *J. Chem. Phys.* **25**, 693 (1956).
- ³⁵ L. X. Benedict, N. G. Chopra, M. L. Cohen, A. Zettl, S. G. Louie, and V. H. Crespi, *Chem. Phys. Lett.* **286**, 490 (1998).
- ³⁶ R. Zacharia, H. Ulbricht, and T. Hertel, *Phys. Rev. B* **69**, 155406 (2004).
- ³⁷ J.-C. Charlier, X. Gonze, and J.-P. Michenaud, *Europhys. Lett.* **29**, 43 (1995).
- ³⁸ S. B. Trickey, F. Müller-Plathe, G. H. F. Diercksen, and J. C. Boettger, *Phys. Rev. B* **45**, 4460 (1992).
- ³⁹ H. Rydberg, M. Dion, N. Jacobson, S. E., P. Hyldgaard, S. I. Simak, D. C. Langreth, and B. I. Lundqvist, *Phys. Rev. Lett.* **91**, 126402 (2003).
- ⁴⁰ D. P. DiVincenzo, E. J. Mele, and N. A. W. Holzwarth, *Phys. Rev. B* **27**, 2458 (1983).
- ⁴¹ M. C. Schabel and J. L. Martins, *Phys. Rev. B* **46**, 7185 (1992).
- ⁴² Z. Liu, J. Z. Liu, Y. Cheng, Z. Li, L. Wang, and Q. Zheng, *Phys. Rev. B* **85**, 205418 (2012).